DEVELOPMENTAL BIOLOGY

Phosphorylation by Aurora kinase A facilitates cortical-cytoplasmic dynamics of Par-3 in asymmetric division of radial glia progenitors

Jason Q. Garcia[1,2]†, Vincent Mouilleau[1], Henry Ng[2,3], Xiang Zhao[1,4], David O. Morgan[2,3], Su Guo[1,2,5]*

During asymmetric cell division (ACD) of radial glia progenitors (RGPs), the cortical polarity regulator Par-3 is detected in the cytoplasm colocalizing with dynein and Notch ligand DeltaD (Dld). What drives Par-3 to the cytoplasm and its impact on RGP ACD remain unknown. Here, we visualize cytoplasmic Par-3 using in vivo time-lapse imaging and find that Ser^{954} of zebrafish Par-3 is phosphorylated by Aurora kinase A (AurkA) in vitro. Expression of the nonphosphorylated mutant Par-3^{S954A} dominant negatively affects embryonic development, reduces cytoplasmic Par-3, and disrupts the anteroposterior asymmetry of cortical Par-3 and Dld endosomes and, in turn, daughter cell fate. AurkA in mitotic RGPs shows dynamic pericentrosomal distribution that transiently colocalizes with cortical Par-3 preferentially on the posterior side. AurkA is both necessary and sufficient to increase cytoplasmic while decreasing cortical Par-3, disrupts Par-3 cortical asymmetry, and perturbs polarized Dld endosome dynamics. These findings suggest that AurkA regulates Par-3 cortical-cytoplasmic dynamics that is critical for ACD and daughter cell fate.

INTRODUCTION

During early brain development, radial glia progenitors (RGPs), the principal vertebrate neural stem cells, undergo asymmetric cell division (ACD) to generate two distinct daughter cells: One maintains stemness (self-renewal), and the other becomes a differentiating neuron. ACD is essential for generating diverse differentiated cell types while maintaining the stem cell population. Therefore, disruption of this process can lead to early developmental defects and cancer (*1*–*5*). Elucidating the mechanisms that regulate ACD is fundamental for understanding both basic biology and disease mechanisms.

ACD requires the establishment of a polarity axis in relation to the cleavage plane in the mother cell. The evolutionarily conserved partitioning defective protein (Par) complexes, originally discovered in *Caenorhabditis elegans* (*6*–*9*), play a crucial role in regulating these processes. In the developing vertebrate forebrain, Par-3, also known as PARD3 in humans and Bazooka in *Drosophila*, is localized at the apical cortex of neuroepithelial cells, which are precursors of RGPs (*10*–*14*). During active neurogenesis, most RGPs divide along the anterior-posterior (A-P) embryonic axis (not the apical basal axis), thereby distributing the apical Par-3 to both daughter cells (*1*, *5*, *13*–*22*).

Par-3 was thought to function exclusively at the cell cortex until recently. Studies in the developing zebrafish forebrain during active neurogenesis have revealed that apically localized Par-3 in dividing RGPs becomes further polarized along the A-P axis and is preferentially segregated to the posterior self-renewing daughter (*14*, *23*). Moreover, Par-3 is detected in the cytoplasm to form a complex with Dlic1 (dynein intermediate light chain 1) on the Notch ligand DeltaD (Dld)–containing endosomes and is required for the asymmetric segregation of these endosomes (*23*). Polarized dynamics of Notch signaling endosomes was first observed during ACD of *Drosophila* neural progenitors (*24*, *25*), suggesting that it is evolutionarily conserved. Both zebrafish and mammalian RGPs undergo ACD to generate daughter cells with asymmetric activity of Notch signaling (*13*–*17*), a key regulator of cell fate decisions (*18*, *19*). Disruption of Par-3 results in a loss of Notch asymmetry (*13*, *14*) in daughter cells, which may contribute to tumorigenesis and cancer metastasis (*1*, *5*, *20*–*22*).

Together, these findings raise the following questions: What mechanisms drive the presence of Par-3 in the cytoplasm? How does such regulation contribute to the establishment of cell polarity and ensuing daughter cell fate?

Phosphorylation, a crucial posttranslational modification in biological systems, has a profound impact on cellular processes, signaling cascades, and organismal development. Phosphorylation of Par-3 by atypical protein kinase C (aPKC) (*26*–*30*), Par-1 (*8*, *31*), and PLK-1 (Polo-like kinase–1) (*32*) has been studied mostly in invertebrates and, on some occasions, cultured mammalian cells. The cell cycle–dependent Aurora kinase A (AurkA), highly expressed in the nervous system (*33*), emerges as a notable player in cell cycle regulation. Studies have linked Aurora kinases with PAR network activation in *C. elegans* (*34*) and with Par-6 during ACD in *Drosophila* neuroblasts (*35*). Mammalian AurkA has been shown to phosphorylate human PARD3 at Ser^{962} in axon formation of cultured hippocampal neurons (*36*).

In this study, we carried out in vivo time-lapse imaging to observe the dynamics of Par-3 in RGPs using an established Par-3–green fluorescent protein (GFP) reporter (*10*–*12*, *23*). We observed that Par-3 appeared in the cytoplasm upon mitotic entry. We therefore

---

[1]Department of Bioengineering and Therapeutic Sciences, University of California, San Francisco, San Francisco, CA 94143, USA. [2]Tetrad Graduate Program, University of California, San Francisco, San Francisco, CA 94143, USA. [3]Department of Physiology, University of California, San Francisco, San Francisco, CA 94143, USA. [4]Chan Zuckerberg Biohub, San Francisco, CA 94158, USA. [5]Programs in Biological Sciences and Quantitative Biosciences, Institute of Human Genetics, Kavli Institute for Fundamental Neuroscience, Bakar Aging Research Institute, University of California, San Francisco, San Francisco, CA 94143, USA.
*Corresponding author. Email: su.guo@ucsf.edu
†Present address: Department of Neurology, Columbia University, New York, NY 10032, USA.

investigated the cell cycle–dependent kinase AurkA, which has two consensus phosphorylation motifs in zebrafish Par-3. We showed that the presence of Par-3 in the cytoplasm was facilitated by AurkA phosphorylation at Ser^{954} of Par-3. Furthermore, we detected a transient colocalization of AurkA and cortical Par-3 on one side of the anaphase RGPs, correlating with the directionality of Par-3 cortical asymmetry along the A-P axis; colocalization of AurkA and cortical Par-3 showed enrichment on the posterior side. Both transient inhibition and overexpression of AurkA altered the Par-3 cytoplasmic and cortical presence, disrupted its cortical asymmetry, and perturbed the polarized dynamics of Dld endosomes. Overall, our findings reveal a role of AurkA in phosphorylating Par-3, promoting the Par-3 cytoplasmic presence in mitotic RGPs, and neural progenitor fate.

RESULTS

In vivo time-lapse imaging uncovers the dynamics of cytoplasmic Par-3 in mitotic RGPs

Using label retention expansion microscopy, we previously detected Par-3 in the cytoplasm in complexes with the dynein subunit Dlic1 and Dld endosomes in mitotic RGPs (*23*). In the developing zebrafish forebrain, mitotic RGPs that divide along the A-P axis display three modes of divisions: (i) Most RGPs asymmetrically segregate cortical Par-3 and Dld endosomes to the posterior daughter. (ii) A small portion of RGPs asymmetrically segregates cortical Par-3 and Dld endosomes to the anterior daughter. (iii) Another small portion of RGPs shows symmetrical distribution of cortical Par-3 and Dld endosomes to both daughters (Fig. 1A).

To better understand the cytoplasmic and cortical Par-3, we carried out in vivo time-lapse imaging. The mRNAs encoding Par-3-GFP and histone monomeric red fluorescent protein (RFP; H2B-mRFP) (marks cell nuclei) were microinjected into one cell of 16- to 32-cell *Tg[ef1a-MyrTdTomato]* (marks cell membranes) embryos to achieve sparse labeling. Care was taken to deliver the Par-3-GFP mRNA at a concentration that does not affect cell polarity, as previously described (*10*–*12*, *23*). Subsequently, the Dld antibody conjugated to a fluorophore was microinjected into the brain ventricle at 22 hours postfertilization (hpf) to label Dld endosomes, as previously described (*23*, *37*–*39*). Live imaging was performed at ~24 to 30 hpf (Fig. 1B).

Punctate GFP signals were observed in the cytoplasm of mitotic RGPs at around the metaphase (Fig. 1, C and D, movie S1, and fig. S1). Compared to cortical Par-3, cytoplasmic Par-3 was at a much lower level. Consistent with previous expansion microscopy data (*23*), colocalization of the GFP signal with Dld endosomes was observed (Fig. 1C, insets, and fig. S1). Intriguingly, cytoplasmic Par-3-GFP appeared emanating from the apical domain and showed enrichment on the posterior side readily observable at the metaphase (Fig. 1D and movie S1). The low signal-to-noise ratio of cytoplasmic Par-3-GFP, however, made the quantification of its cytoplasmic asymmetry challenging. Together, these qualitative observations are consistent with a model postulating the derivation of cytoplasmic Par-3 from the cortical pool.

To better visualize the dynamics of cytoplasmic Par-3-GFP, we reasoned that knocking down endogenous Par-3, which is not visible by live imaging, and replacing it with exogenously provided Par-3-GFP should enhance the detection of cytoplasmic Par-3-GFP. We coinjected a validated Par-3 morpholino (MO) antisense oligonucleotide (*11*) with MO-resistant Par-3-GFP mRNAs as described above. In vivo time-lapse imaging of mitotic RGPs unveiled more intense Par-3-GFP signal in the cytoplasm. Intriguingly, cytoplasmic Par-3-GFP appeared as part of a large assembly that was decorated with many Dld endosomes. As mitotic RGPs progressed through the cell cycle, this large assembly appeared to be pushed to the apical side by the cleavage furrow and then quickly moved toward the posterior (Fig. 1, E and F, movie S2, and fig. S1). Together, in vivo time-lapse imaging of Par-3-GFP and Dld endosome dynamics provides qualitative data that support a model showing that cytoplasmic Par-3 colocalizes with Dld endosomes in a large assembly that undergoes directional movement toward the posterior side in mitotic RGPs.

Systemic expression of Par-3^{S954A} dominantly interferes with embryonic brain development

To build on these qualitative observations and to understand the mechanisms that drive the presence of Par-3 in the cytoplasm, we turned to phosphorylation. Par-3 has many established and predicted phosphorylation sites, which can be visualized using the UniProt database. In this study, we focused on two serines, Ser^{227} and Ser^{954} in zebrafish Par-3, which are predicted phosphorylation sites of AurkA in the consensus RX(S/T)(L/V) motif and are conserved across vertebrates (Fig. 2A) (*36*, *40*, *41*).

Given that cytoplasmic Par-3-GFP became detectable at around the metaphase in mitotic RGPs, we sought to determine whether phosphorylation of these two serines by the cell cycle–dependent kinase AurkA plays a role in driving the presence of Par-3 in the cytoplasm. Precise genome editing of single amino acids has been reported in zebrafish (*42*), but the overall efficiency remains low and is highly dependent on having efficacious single guide RNAs near the desired target sites. As we need to target two serines in different regions of Par-3, this becomes considerably challenging and moreover carries the uncertainty whether such modification may cause early embryonic defects, making the interpretation of RGP phenotypes difficult. We therefore decided to use an alternative approach. Serine-to-alanine and serine-to-aspartic acid mutations were introduced into Par-3-GFP. The mRNAs encoding these mutated forms of Par-3 were microinjected into one-cell stage embryos (for ubiquitous expression) or one cell of the 16- to 32-cell stage (for sparse expression) (Fig. 2B). For the former, embryos were raised to 28 hpf and their brain morphological phenotypes were scored using a phenotype rubric (fig. S2B). We observed that while Par-3-GFP– or Par-3^{SD}-GFP–injected embryos appeared largely normal, Par-3^{SA}-GFP–injected embryos showed defects in brain morphology similar to Par-3 morphants. Further analysis of individual serine mutations uncovered that Par-3^{S954A}-GFP–injected but not Par-3^{S227A}-GFP–injected embryos were defective (Fig. 2, C and D), suggesting that Ser^{954} is the key residue. Together, systemic expression of Par-3^{S954A}-GFP dominantly interferes with the endogenous Par-3 function, leading to defects in embryonic brain development. These data suggest that phosphorylation of Par-3 at Ser^{954} is critical for the Par-3 function.

Sparsely expressed Par-3^{S954A} displays decreased cytoplasmic presence in mitotic RGPs

To determine whether phosphorylation of these two serines is critical for Par-3 dynamics in mitotic RGPs, we coinjected H2B-RFP with different forms of Par-3 mRNAs into one cell of 16- to 32-cell

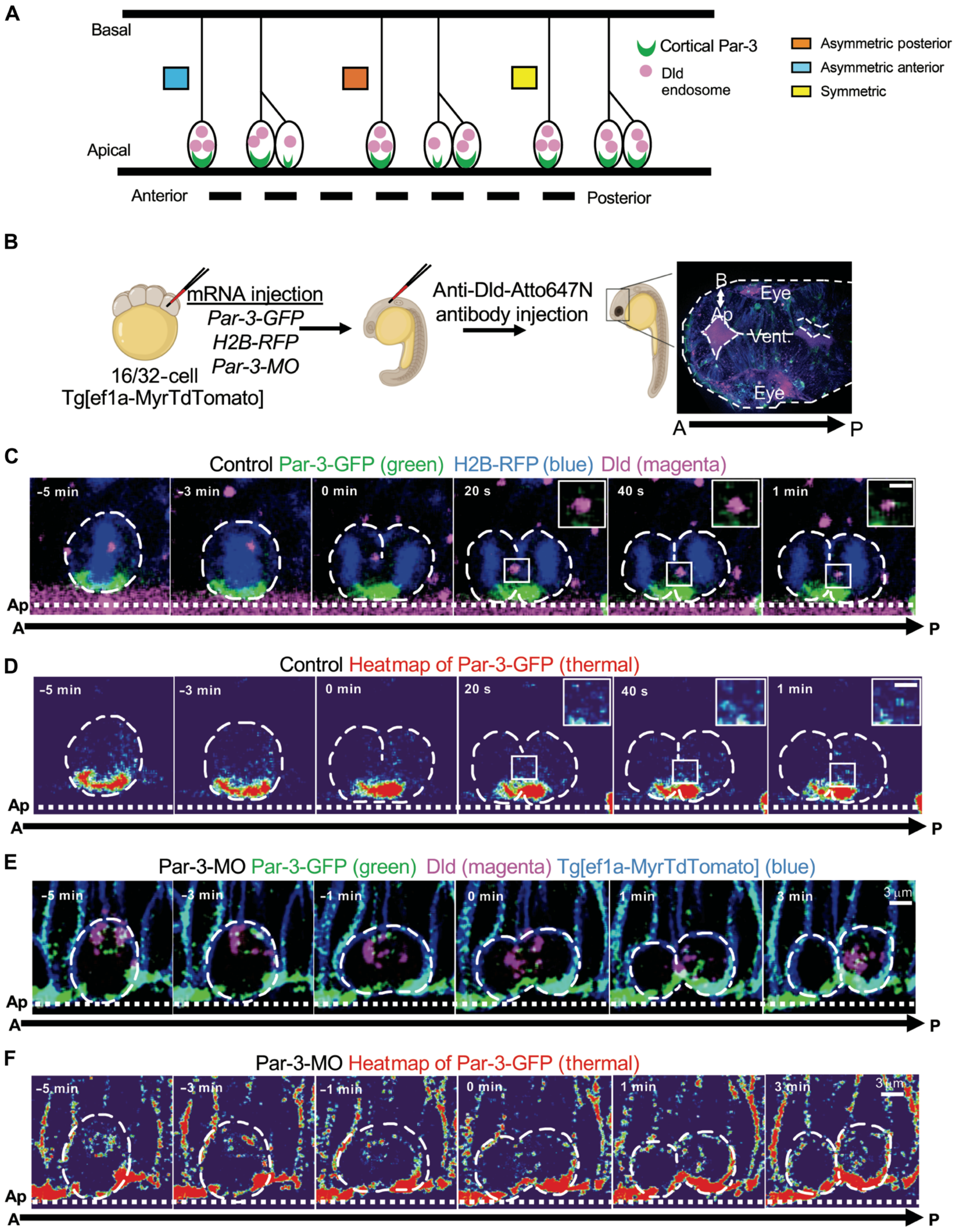

Fig. 1. In vivo time-lapse imaging of cytoplasmic Par-3 in mitotic RGPs. (**A**) Schematic of RGPs undergoing ACD in the developing zebrafish forebrain. While there is heterogeneity during ACD of RGPs, there is a preferential distribution of cortical Par-3 to the posterior daughter cell. (**B**) Experimental schematic. Embryos are injected with mRNAs (~200 pg) at the 16/32-cell stage to achieve sparse labeling, followed by Dld antibody uptake at 20 hpf and confocal imaging at 24 hpf. The membrane is marked with Tg[ef1a-MyrTdTomato] embryos (pseudocolored in blue), and DNA is marked by H2B-RFP (pseudocolored in blue) and Par-3-GFP (green). The time-lapse sequence of all images shown is the maximal intensity projection (MIP) of three confocal *z*-stacks (1-μm *z*-step). The time of −3 min denotes the metaphase. The time interval between each volume of *z*-stacks is 20 s, and the total acquisition time is 30 min. (**C**) Dynamics of internalized Dld and Par-3-GFP in mitotic RGPs. Insets visualize cytoplasmic Par-3 and Dld colocalization during live imaging in RGPs. (**D**) Dynamics of Par-3-GFP (GFP only by the heatmap) in mitotic RGPs. (**E**) One- to four-cell stage Tg[ef1a-MyrTdTomato] embryos (pseudocolored in blue) were injected with 4 ng of *par-3* MO and 400 pg of Par-3-GFP, followed by the Dld antibody uptake assay and live confocal imaging. Time-lapse sequence of images showing the dynamics of internalized Dld and Par-3-GFP in mitotic RGPs. The time of 3 min denotes the telophase. The time interval between each volume of *z*-stacks is 30 s, and the total acquisition time is 30 min. All images shown are the MIP of three confocal *z*-stacks (1-μm *z*-step). (**F**) Dynamics of Par-3-GFP (GFP only by the heatmap) in mitotic RGPs. Ap, apical; A, anterior; B, basal; P, posterior; Vent., ventricle. For detailed statistics, see table S1.

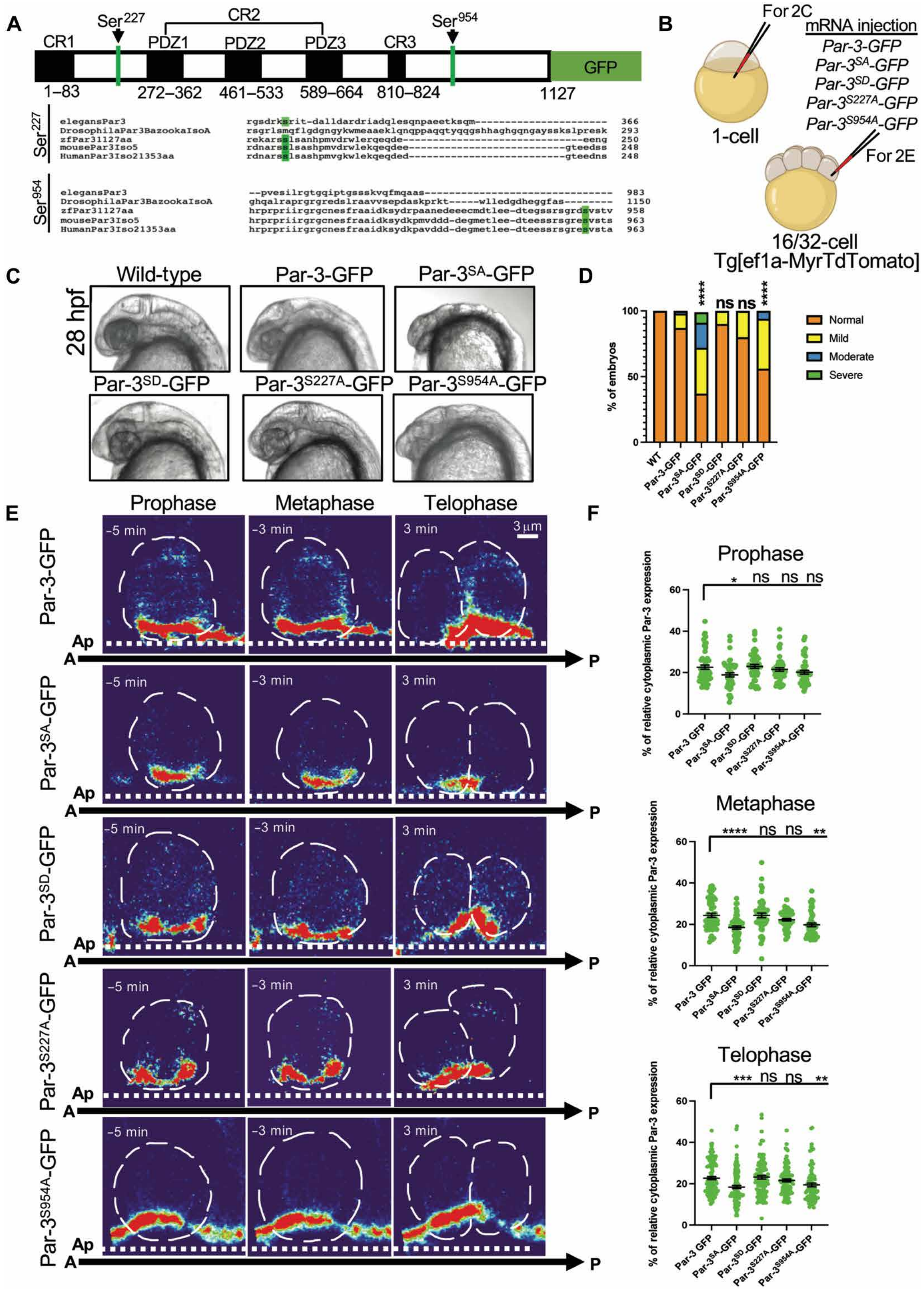

Fig. 2. Expression of Par-3^{S954A} dominantly interferes with embryonic brain development and cytoplasmic Par-3 localization in RGPs. (**A**) Par-3 consists of three conserved regions (CRs), the oligomerization domain (CR1), the three PDZ domains (CR2), and the aPKC binding domain (CR3). The predicted AurkA phosphorylation sites are located at Ser^{227} and Ser^{954} (green), which are conserved across vertebrates. (**B**) Experimental schematic of mRNA injection into one-cell or 16/32-cell stage zebrafish embryos. (**C**) Images of embryonic brain morphology at ~28 hpf. Images were taken at 200× on the Zeiss compound microscope. (**D**) Quantification. Phenotyping rubrics are described in fig. S2. (**E**) Time-lapse sequence of images showing Par-3 and Par-3 phospho mutants (GFP only in the heatmap) in mitotic RGPs at the prophase, metaphase, and telophase. (**F**) Quantification. Relative cytoplasmic Par-3 expression was measured at the prophase, metaphase, and telophase using Fiji. One-way ANOVA test with a post hoc comparison to control (Par-3-GFP). $*P < 0.05$, $**P < 0.01$, $***P < 0.001$, and $****P < 0.0001$; ns, not significant. For detailed statistics, see table S1. See table S2 for the representative image signal values compared to the median signal values.

stage *Tg[ef1a-MyrTdTomato]* embryos (Fig. 2B). By sparse labeling, we were able to follow individual RGPs using in vivo time-lapse imaging in embryos with normal brain morphology. Because of considerable heterogeneity of RGPs, we measured relative reporter expression normalized to the total reporter expression in each cell. The quantification method for cortical versus cytoplasmic Par-3-GFP fluorescence intensity in RGPs is described in fig. S2A. We found that in Par-3^{SA}-GFP– and Par-3^{S954A}-GFP–injected embryos compared to Par-3-GFP–injected ones, mitotic RGPs showed significantly decreased cytoplasmic Par-3-GFP at the metaphase and telophase and increased cortical Par-3-GFP, whereas Par-3^{SD}-GFP– and Par-3^{S227A}-GFP–injected embryos had no significant difference compared to controls (Fig. 2, E and F; fig. S2, C and D; and movies S3 to S7).

We also analyzed the absolute cytoplasmic Par-3 without normalization to the total reporter expression in each RGP shown in Fig. 2. The results showed no clear patterns (fig. S3), suggesting that measuring relative cytoplasmic Par-3 helps normalize variables either intrinsic to each RGP or because of differences of exogenously expressed Par-3 reporter in each RGP despite the highly controlled delivery of the amount of reporter mRNAs at an early developmental stage (one cell of the ~16- to 32-cell stage).

Sparsely expressed Par-3^{S954A} is defective in A-P cortical asymmetry and dominantly interferes with the formation and polarized dynamics of Dld endosomes in mitotic RGPs

To further understand the effect of Par-3^{S954A} in mitotic RGPs, we simultaneously tracked the dynamics of the Par-3 reporter and internalized Dld using in vivo time-lapse imaging (Fig. 3A). In control (Par-3-GFP–expressing) embryos, both Par-3 and Dld were preferentially segregated into the posterior daughter (Fig. 3B), as previously reported (*23*). In Par-3^{SA}-GFP–expressing embryos, not only the cytoplasmic Par-3^{SA}-GFP signal was reduced, but also the cortical Par-3^{SA}-GFP asymmetry was disrupted (Fig. 3C). These disruptions were not observed in Par-3^{SD}-GFP– and Par-3^{S227A}-GFP–expressing embryos (Fig. 3, D and E) but were similarly observed in Par-3^{S954A}-GFP–expressing embryos (Fig. 3F). While Par-3 cortical asymmetry was often observable at the anaphase, because of the lack of a clear boundary between future daughter cells, we performed quantifications at the telophase using previously established methods (*13*, *14*, *23*) (see Materials and Methods for details). Both internalized Dld endosomes and Par-3-GFP at the telophase showed a significantly reduced asymmetry in Par-3^{SA}-GFP– and Par-3^{S954A}-GFP–expressing embryos (Fig. 3, G and H). In addition, a decrease in internalized Dld was observed in Par-3^{SA}-GFP– and Par-3^{S954A}-GFP–expressing embryos compared to controls (Fig. 3I). A similar decrease in internalized Dld expression was also observed in the Par-3 morphants compared to control MO (fig. S4), suggesting that these forms of nonphosphorylated Par-3 dominantly interfere with Dld endocytosis.

Like what we did above, we analyzed the absolute cytoplasmic Par-3 without normalization to the total reporter expression in each RGP shown in Fig. 3. The results again showed no clear patterns (fig. S5), suggesting that measuring relative cytoplasmic Par-3 is needed to observe the significant intergroup differences as shown in Fig. 3. Together, these findings suggest that phosphorylation at Ser^{954} plays a role in promoting the cytoplasmic presence and cortical asymmetry of Par-3, as well as Dld asymmetry during ACD in RGPs.

Systemic expression of Par-3^{S954A} dominantly interferes with progenitor-neuron fate specification in the developing forebrain

Next, we investigated the impact of Par-3 phosphorylation at Ser^{954} on cell fate in the developing forebrain through a 5-ethynyl-2′-deoxyuridine (EDU) labeling experiment. We expressed Par-3-GFP or Par-3^{S954A}-GFP in wild-type (WT) embryos by microinjecting them at the one-cell stage. Embryos were then allowed to develop until 18 hpf, followed by injection of 50 μM EDU into the yolk sac, as previously described (*43*). Embryos were raised and fixed at 24 and 36 hpf, and samples were prepared for cryosectioning and immunostaining for HuC (neuronal marker) and EDU (proliferation marker) using Click it-EDU chemistry labeling (Fig. 4A).

Quantification of EDU-positive cells at 24 and 36 hpf showed no difference among WT, full-length Par-3-GFP–expressing, and Par-3^{S954A}-GFP–expressing embryos (Fig. 4, B to H and K), suggesting that the expression of Par-3^{S954A} does not affect progenitor entry to the S phase. However, we found a significant decrease in the ratio of EDU^+HuC^+/EDU^+ (Fig. 4, B to G, J, and M) cells (i.e., decrease in neurons derived from EDU-labeled progenitors) and a corresponding increase in the ratio of EDU^+HuC^-/EDU^+ cells (Fig. 4, B to G, I, and L) (i.e., increase in progenitors derived from EDU-labeled progenitors) in Par-3^{S954A}-GFP–expressing embryos compared to full-length Par-3-GFP–expressing and WT embryos. These results suggest that phosphorylation of Par-3 at Ser^{954} is critical for promoting progenitor cell cycle exit and differentiation into neurons.

AurkA phosphorylates zebrafish Par-3 at Ser^{954} in vitro

Ser^{954} in zebrafish Par-3 is orthologous to Ser^{962} in human PARD3, which is shown to be phosphorylated by AurkA in the context of axon formation of cultured hippocampal neurons (*36*). To determine whether Ser^{954} in zebrafish Par-3 is phosphorylated by AurkA, we performed an in vitro kinase assay using in vitro–translated forms of Par-3 (Par-3-GFP, Par-3^{S227A}-GFP, Par-3^{S954A}-GFP, and Par-3^{SA}-GFP) and recombinant AurkA (Fig. 5A). We first verified that zebrafish Par-3 was phosphorylated by AurkA in vitro (fig. S6). We then used ^{35}S labeling to quantify the amount of in vitro–translated proteins and used this for normalization of the detected phosphorylation signals (Fig. 5, B and C). We uncovered significantly reduced phosphorylation for Par-3^{S954A}-GFP and Par-3^{SA}-GFP but not Par-3^{S227A}-GFP compared to Par-3-GFP (Fig. 5D). Together, our biochemical analysis demonstrates that AurkA phosphorylates Par-3 at Ser^{954} in vitro.

In vivo time-lapse imaging reveals a transient colocalization of AurkA and cortical Par-3 that correlates with the directionality of Par-3 cortical asymmetry in mitotic RGPs

To characterize the relationship between AurkA and Par-3 in vivo, we microinjected mRNAs encoding 100 pg of Centrin-GFP (or Par-3-GFP) and 50 pg of mCherry-AurkA into one cell of 16/32-cell stage *Tg[b-actin2:H2B-HaloTag]* (marking nuclei) embryos. We then incubated the embryos for 2 hours in Halo ligand 646 to label the nuclei before time-lapse imaging of mitotic RGPs (Fig. 6A). Consistent with previous studies (*33*, *44*), we observed AurkA localization near the centrosomes in mitotic RGPs and the signal disappeared shortly after the completion of mitosis (fig. S7 and movie S8).

Intriguingly, this pericentrosomal AurkA underwent dynamic movements. We observed that mCherry-AurkA and Par-3-GFP

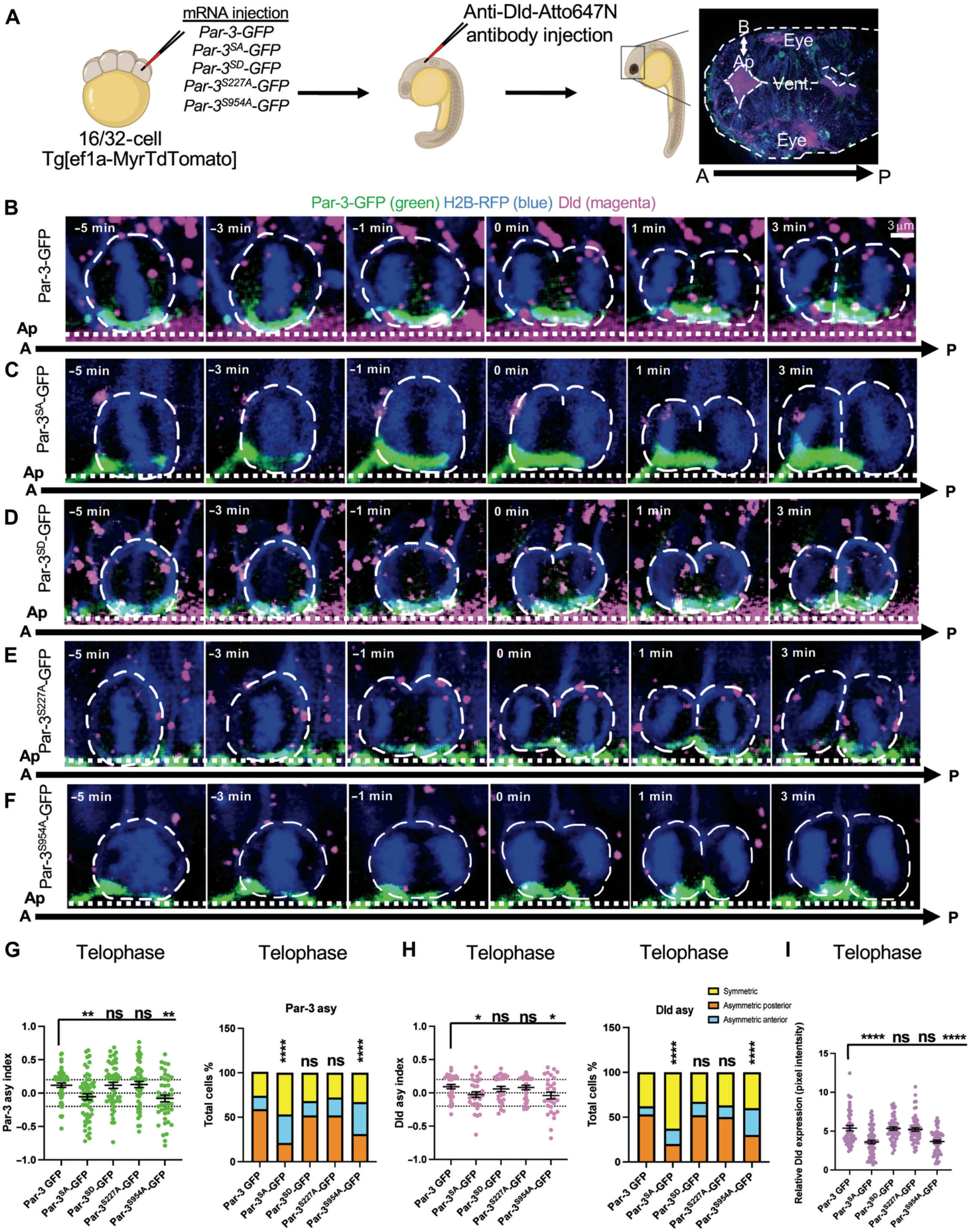

Fig. 3. Par-3^{S954A} displays reduced posterior cortical asymmetry and dominantly interferes with polarized Dld endosome dynamics in mitotic RGPs. (**A**) Experimental schematic. (**B** to **F**) Time-lapse sequence of images showing the dynamics of internalized Dld and Par-3$^{(SA, SD, S227A, or S954A)}$-GFP in mitotic RGPs. The time of 3 min denotes the telophase when asymmetry indices are calculated. The time interval between each volume of *z*-stacks is 20 s, and the total acquisition time is 30 min. All images shown are MIP of three confocal *z*-stacks (1-μm *z*-step). (B) Par-3-GFP: Both internalized Dld and Par-3 are asymmetrically segregated to the posterior daughter shortly after division. (C) Par-3^{SA}-GFP: disrupted internalized Dld and Par-3 asymmetry shortly after division compared to Par3-GFP. (D) Par-3^{SD}-GFP: comparable to Par-3-GFP. (E) Par-3^{S227A}-GFP: comparable to Par-3-GFP. (F) Par-3^{S954A}-GFP: similar to Par-3^{SA}-GFP. (**G** to **I**) Quantification. Scatter plot showing asymmetry indices in telophase RGPs. (G) Asymmetry indices of different forms of Par-3-GFP. The dotted lines indicate the threshold of |0.2| for calling asymmetry. (H) Asymmetry indices of internalized Dld (right) in RGPs expressing different forms of Par-3. (I) Telophase RGPs: The relative Dld expression graph reveals a decrease in Dld expression in Par-3^{SA}-GFP and Par-3^{S954A}-GFP compared to control Par-3-GFP. *$P < 0.05$, **$P < 0.01$, ***$P < 0.001$, and ****$P < 0.0001$; ns, not significant. For detailed statistics, see table S1. See table S2 for the representative image signal values compared to the median signal values.

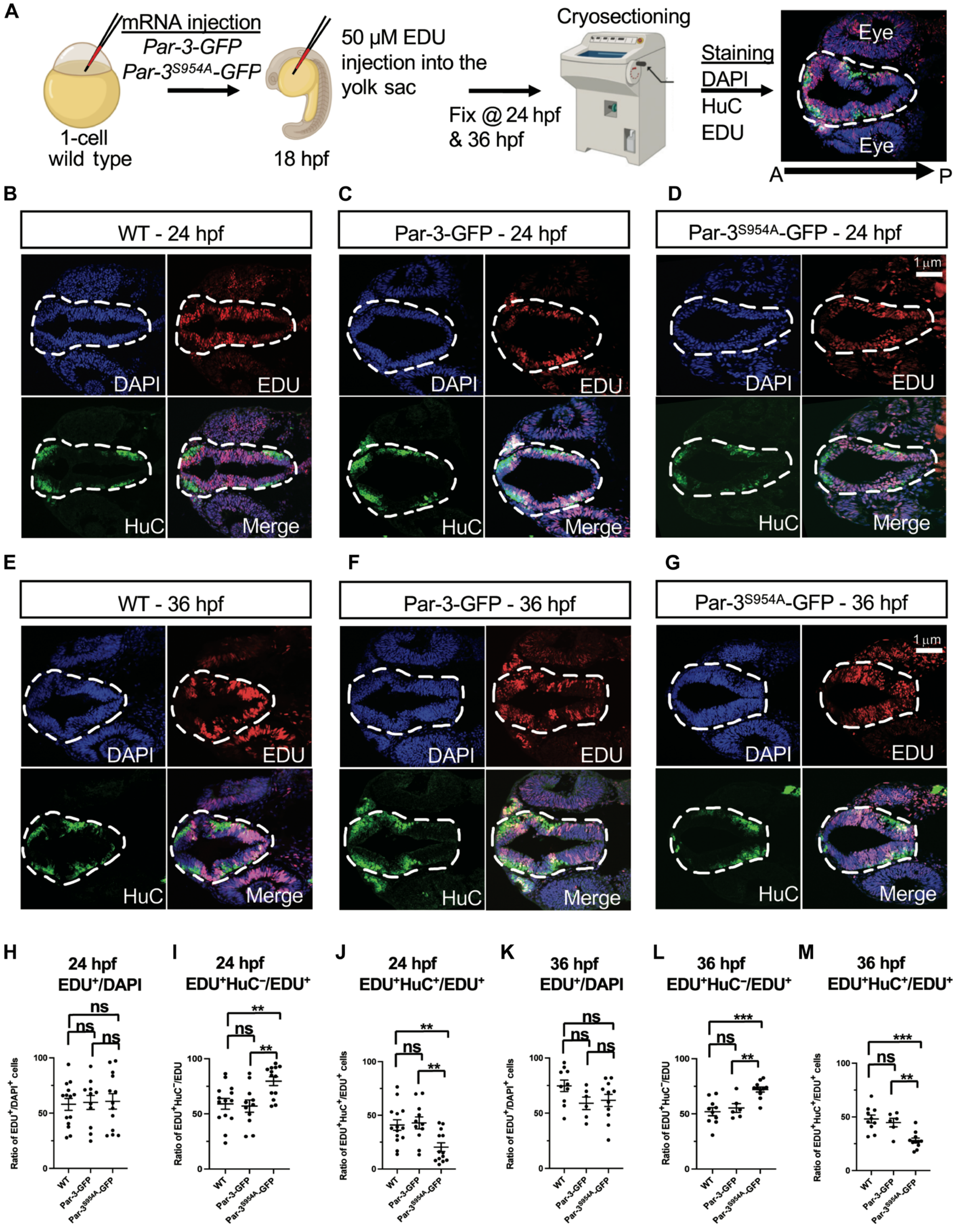

Fig. 4. Par-3^{S954A} dominantly interferes with progenitor cell fate during active neurogenesis. (**A**) Experimental schematic: one-cell injection of mRNA (200 pg) of Par-3-GFP and Par-3^{S954A}-GFP into WT embryos. Embryos were injected with 50 μM EDU at 18 hpf into the yolk sac, followed by fixation, cryosectioning, and confocal microscopy at 24 and 36 hpf. (**B** to **G**) WT, Par-3-GFP, and Par-3^{S954A}-GFP 24-hpf [(B) to (D)] and 36-hpf [(E) to (G)] cryosectioned images as single *z*-stack projection (1 μm) stained with 4′,6-diamidino-2-phenylindole (DAPI), anti-HuC, and anti-EDU. The dash line highlights the forebrain region of interest. (**H** to **M**) Quantification. (H) 24-hpf EDU$^+$/DAPI comparing WT, Par-3-GFP, and Par-3-^{S954A}-GFP. (I) 24-hpf EDU$^+$HuC$^-$/EDU$^+$ comparing WT, Par-3-GFP, and Par-3-^{S954A}-GFP. (J) 24-hpf EDU$^+$HuC$^+$/EDU$^+$ comparing WT, Par-3-GFP, and Par-3-^{S954A}-GFP. (K) 36-hpf EDU$^+$/DAPI comparing WT, Par-3-GFP, and Par-3-^{S954A}-GFP; $P > 0.1229$, ns; WT versus Par-3-GFP. (L) 36-hpf EDU$^+$HuC$^-$/EDU$^+$ comparing WT, Par-3-GFP, and Par-3-^{S954A}-GFP. (M) 36-hpf EDU$^+$HuC$^+$/EDU$^+$ comparing WT, Par-3-GFP, and Par-3-^{S954A}-GFP. $^*P < 0.05$, $^{**}P < 0.01$, $^{***}P < 0.001$, and $^{****}P < 0.0001$; ns, not significant. For detailed statistics, see table S1. See table S2 for the representative image signal values compared to the median signal values.

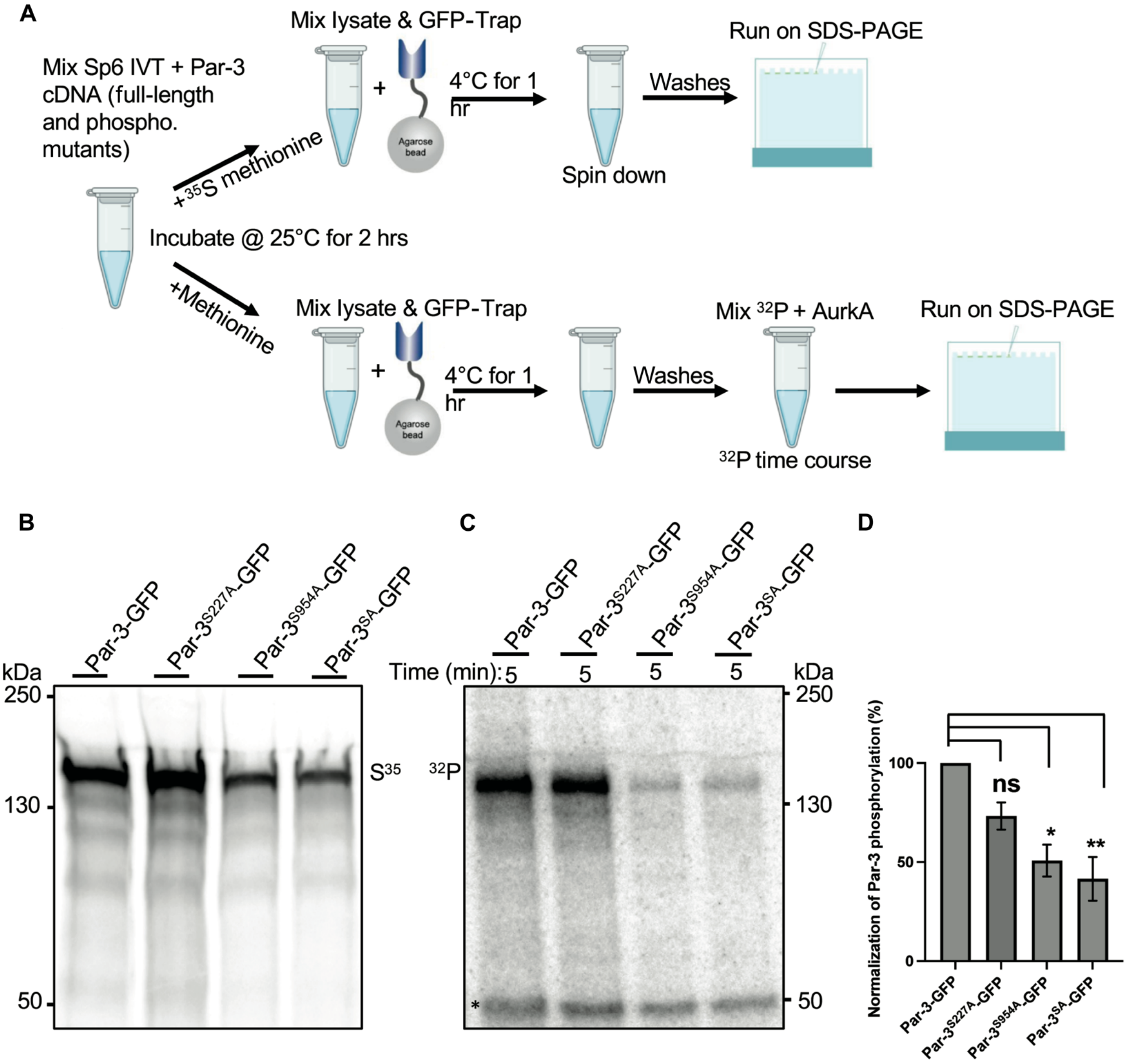

Fig. 5. AurkA directly phosphorylates Par-3 at Ser^{954}. (**A**) Experimental schematic: in vitro–translated Par-3-GFP or Par-3$^{(SA,\ S954A,\ SD,\ or\ S227A)}$-GFP was immunoprecipitated with GFP-Trap agarose beads and mixed with 250 nmol of AurkA and [^{32}P]-ATP. Samples were analyzed by SDS-PAGE and autoradiography. hr, hour. (**B**) Radiolabeled [^{35}S]. Samples were removed and processed by SDS-PAGE/autoradiography. (**C**) Unlabeled Par-3-GFP immunoprecipitants were incubated with AurkA and [^{32}P]-ATP for 5 min, and reaction products were analyzed by SDS-PAGE and autoradiography. Par-3, 150 kDa. *AurkA autophosphorylation, 50 kDa. (**D**) Quantification of phosphorylation, normalized to the amount of Par-3 protein. *$P < 0.05$, **$P < 0.01$, ***$P < 0.001$, and ****$P < 0.0001$; ns, not significant. For detailed statistics, see table S1.

were in proximity at the metaphase and colocalized at the anaphase in the posterior (Fig. 6B and movie S9) or the anterior sides (Fig. 6C and movie S10). In some RGPs, no such contact was observed (Fig. 6D and movie S11). Next, we asked whether there is a correlation between the side where AurkA colocalized with cortical Par-3 and the directionality of Par-3 cortical asymmetry. We found that among 27 RGPs analyzed, 14 showed AurkA-Par-3 colocalization on the posterior side, 4 showed colocalization on the anterior side, and 9 did not have detectable colocalization. Among the RGPs with AurkA-Par-3 colocalization on the posterior side, 71% had Par-3-GFP asymmetrically segregated to the posterior daughter cell. Among the RGPs with AurkA-Par-3 colocalization on the anterior side, 50% had Par-3-GFP asymmetrically segregated to the anterior daughter cell. In addition, in the cases where no Par-3-AurkA colocalization was detected, 45% of RGPs had Par-3-GFP symmetrically distributed between the two daughter cells (Fig. 6E). Thus, there is a significant correlation between the side of AurkA-Par-3 dynamic colocalization and the side of enriched cortical Par-3 in RGPs. These findings are consistent with the model showing that AurkA phosphorylates Ser^{594} of Par-3, and the side of its colocalization correlates with the directionality of Par-3 cortical asymmetry.

Transient inhibition of AurkA activity decreases cytoplasmic Par-3 and disrupts Par-3 cortical asymmetry and polarized Dld endosome dynamics in mitotic RGPs

Next, we investigated the impact of inhibiting AurkA on mitotic RGPs. Because AurkA is critical for cell cycle progression, we used a specific chemical inhibitor MK-5108 (*45*), which enabled us to perform a loss-of-function experiment in a temporally controllable manner. We microinjected the mRNAs encoding Par-3-GFP

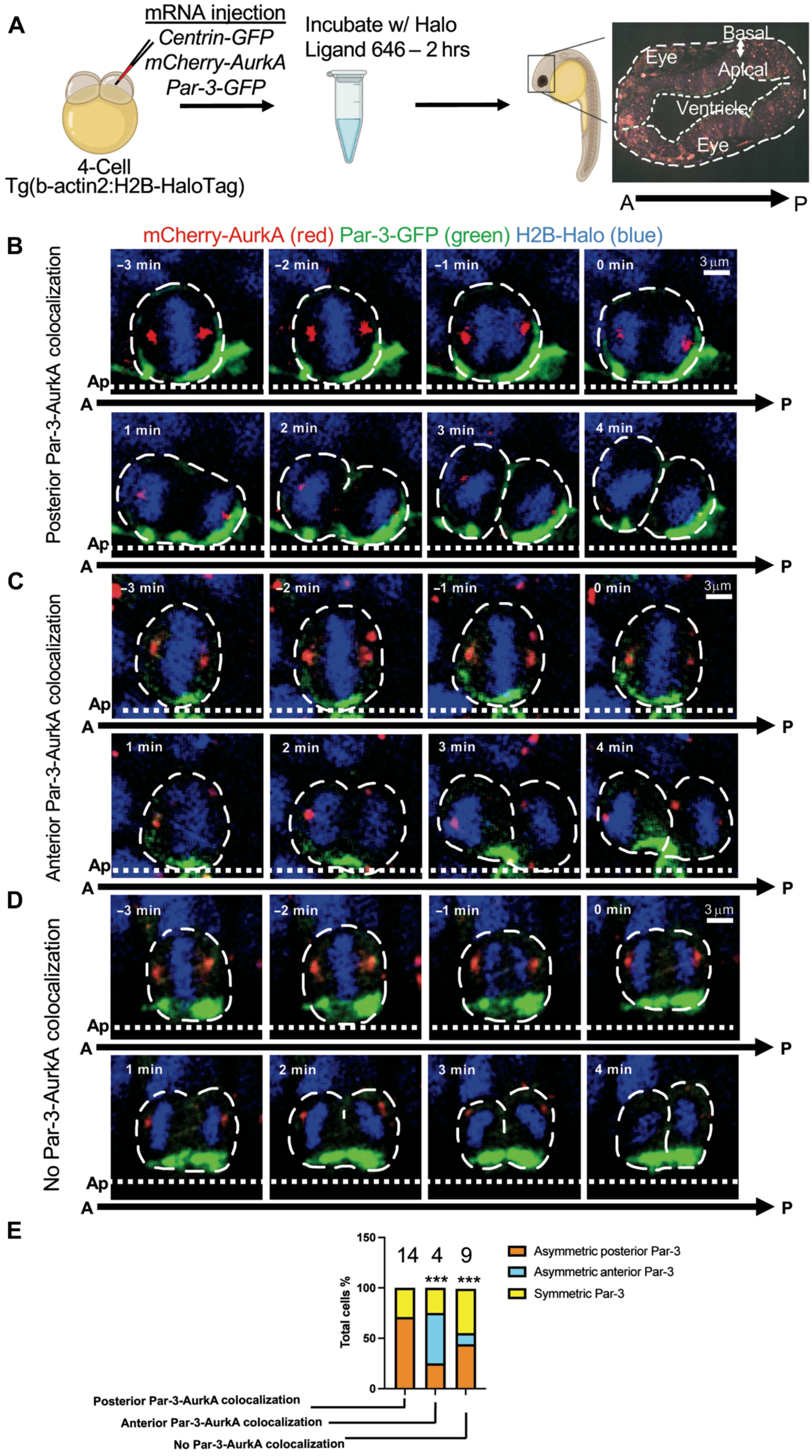

Fig. 6. In vivo time-lapse imaging reveals AurkA dynamics and transient colocalization with Par-3 in mitotic RGPs. (**A**) Experimental schematic: mRNA microinjections into four-cell Tg[b-actin2:H2B-HaloTag] embryos to achieve sparse labeling. Subsequently, embryos were incubated with Halo Tag ligand-Janelia Flour 646 for 2 hours before live imaging. Twenty-four– to 30-hpf embryos are then mounted on a petri dish with a glass cover for live confocal imaging. Confocal image of a 28-hpf zebrafish forebrain (dorsal view) under a 40× objective. The time interval between each volume of *z*-stacks is 20 s, and the total acquisition time is 30 min. All images shown are the maximum MIP of three confocal z-stacks (1-µm *z*-step). (**B** to **D**) In vivo time-lapse imaging of Par-3-GFP and mCherry-AurkA in mitotic RGPs. Arrows indicate AurkA dynamic movements. Par-3-GFP is asymmetrically segregated to the posterior daughter shortly after division, and there is AurkA colocalization toward the posterior side of the cell. (**E**) Quantification. The bar graph illustrates different patterns of Par-3-AurkA colocalization, while Par-3 undergoes asymmetric distribution in RGPs. $*P < 0.05$, $**P < 0.01$, $***P < 0.001$, and $****P < 0.0001$; ns, not significant. For detailed statistics, see table S1.

together with H2B-RFP into one cell of 16- to 32-cell stage embryos to achieve sparse labeling. Subsequently, the Dld antibody was microinjected into the brain ventricle at 20 hpf. Before imaging, embryos were incubated in 1 μM MK-5108 for various periods of time (Fig. 7A). We observed that in the embryos treated with MK-5108 for 50 min, some RGPs underwent cell cycle arrest (39%, $n = 226$ RGPs from eight embryos of two independent experiments), but most were able to complete mitosis. However, in the embryos treated with MK-5108 for 60 min or longer, most RGPs underwent cell cycle arrest (91%, $n = 65$ RGPs from one embryo) (Fig. 7, B to D, fig. S8A, and movie S12). Therefore, we defined 50-min MK-5108 treatment as the best condition to observe the effect of AurkA inhibition without inducing profound cell cycle arrest (Fig. 7C). Inhibition of AurkA decreased the Par-3 cytoplasmic presence while increasing its cortical presence (Fig. 7, D and E). Inhibition of AurkA also impaired Par-3 cortical asymmetry (Fig. 7F) and disrupted polarized Dld endosome distribution (Fig. 7G). Together, these data suggest that AurkA is essential to promote the Par-3 cytoplasmic presence and cortical asymmetry as well as polarized Dld endosome distribution in mitotic RGPs.

Overexpression of AurkA increases the cytoplasmic Par-3 presence and disrupts Par-3 cortical asymmetry and polarized Dld endosome dynamics

We next asked whether overexpression of AurkA might affect Par-3 dynamics and ACD of mitotic RGPs. One group of embryos was injected with 100 pg of mRNAs encoding Par-3-GFP into one cell at the 16- to 32-cell stage to achieve sparse labeling (Fig. 8A). Another group of embryos was injected with 100 pg of Par-3-GFP and 400 pg of mCherry-AurkA mRNAs into one cell at the 16- to 32-cell stage (Fig. 8B, fig. S9A, and movie S13). Because of the lack of an antibody that can recognize zebrafish AurkA, we quantified the mCherry-AurkA fluorescent signal intensity and found that the overexpression condition (i.e., injected with 400 pg of mCherry-AurkA) had a significantly higher signal than the nonoverexpressing condition in Fig. 6 (i.e., injected with 50 pg of mCherry-AurkA), both in the whole RGPs (fig. S10A) and in the pericentrosome area (fig. S10B). Significantly reduced Par-3-GFP in the apical cortex (Fig. 8C) and a corresponding increase in nonapical Par-3-GFP (including both cytoplasmic and basally enriched Par-3) (Fig. 8D) were detected in the embryos injected with mRNAs encoding Par-3-GFP and AurkA compared to those injected with mRNAs encoding Par-3-GFP only.

To determine whether decreased apical Par-3-GFP and increased nonapical Par-3-GFP are dependent on the phosphorylation of Par-3 at Ser^{954} by AurkA, we injected mRNAs encoding Par-3^{S954A}-GFP and AurkA into one cell at 16- to 32-cell stage embryos. We quantified the levels of AurkA overexpression in Par-3-GFP–injected versus Par-3^{S954A}-GFP–injected embryos and found them to be comparable (fig. S10, A and B). In the embryos coinjected with Par-3^{S954A}-GFP and AurkA mRNAs (Fig. 8E and movie S14), Par-3^{S954A}-GFP fluorescence was significantly increased in the apical cortex (Fig. 8F) and correspondingly reduced in the cytoplasm (Fig. 8G) compared to those injected with mRNAs encoding Par-3-GFP and AurkA. Together, these results suggest that AurkA is sufficient to increase the presence of Par-3 in both the cytoplasm and the basal side that is dependent on Ser^{954}, which is phosphorylated by AurkA in vitro.

Last, we asked whether AurkA overexpression might affect Par-3 cortical asymmetry and polarized Dld endosome dynamics. In the embryos expressing Par-3-GFP, the reporter was enriched in the posterior daughter of telophase RGPs. In the embryos expressing Par-3-GFP and AurkA, a significant decrease in asymmetric posterior Par-3-GFP was observed (Fig. 8, H and I), together with a disruption of Dld endosome asymmetry (Fig. 8J). In the embryos expressing Par-3^{S954A}-GFP and AurkA, a significant decrease in asymmetric posterior Par-3^{S954A}-GFP was also observed, likely due to the dominant negative effect of Par-3^{S954A}-GFP (Fig. 8H). Together, these results suggest that the level of Par-3 phosphorylation by AurkA is critical for Par-3 asymmetry in mitotic RGPs: Both too much and too little phosphorylation can lead to disrupted cortical asymmetry of Par-3 and perturbed polarized dynamics of Dld endosomes.

DISCUSSION

The evolutionarily conserved polarity regulator Par-3 has been traditionally studied at the cell cortex for its role in establishing polarity during ACD. Recent discoveries, however, have revealed the presence of Par-3 in the cytoplasm of RGPs (*23*), with clinical implications linking cytoplasmic Par-3 to adverse cancer prognosis (*46*). Despite this association, what drives the presence of Par-3 in the cytoplasm remains poorly understood. In this study, using in vivo time-lapse imaging, molecular genetics, and pharmacological and biochemical approaches, we studied two serines in the predicted AurkA phosphorylation consensus motifs and uncovered a dominant-negative effect of the Ser^{954}→Ala (S954A) mutant form of Par-3. When expressed ubiquitously in WT embryos, this mutant form of Par-3 disrupted embryonic brain development; when expressed sparsely, it did not affect embryonic morphology but interfered with RGP ACD and daughter cell fate specification. We further showed that Ser^{954} of Par-3 was phosphorylated by AurkA in vitro. Although it remains to be determined whether Par-3 is phosphorylated on this site by AurkA in vivo, our data suggest that AurkA is necessary and sufficient to increase the cytoplasmic presence of Par-3 in a Ser^{954}-dependent manner. Both overexpression and inhibition of AurkA as well as expression of the S954A mutant form of Par-3 disrupted Par-3 cortical asymmetry and perturbed polarized Dld endosome dynamics along the A-P axis. On the basis of these findings, we propose a mechanism for the regulation and function of cytoplasmic Par-3 during ACD in RGPs. As RGPs enter mitosis, cell cycle–dependent AurkA becomes active (at least in subsets of RGPs). Through transient colocalization with the apical cortical Par-3 starting at the metaphase (preferentially on the posterior side in most RGPs), AurkA phosphorylates Par-3 to promote its translocation into the cytoplasm, where it interacts with dynein and directs polarized Dld endosome movement in a large assembly toward the posterior side. In the end, cortical Par-3, cytoplasmic Par-3 (together with dynein), and Dld endosomes are asymmetrically segregated to the posterior daughter cell, where they play a crucial role in promoting the progenitor state. When such an asymmetric process was disrupted in the RGPs expressing the dominant-negative Par-3^{S954A}-GFP, a decrease in neurons and a corresponding increase in progenitors were observed (Fig. 8K).

An alternative approach to expressing the dominant-negative Par-3^{S954A}-GFP as we did here is to introduce the S954A mutation into the endogenous *par-3* locus. We did not pursue such an approach in this study because of the low efficiency of currently available CRISPR knockin methods. Moreover, on the basis of the disruption of early

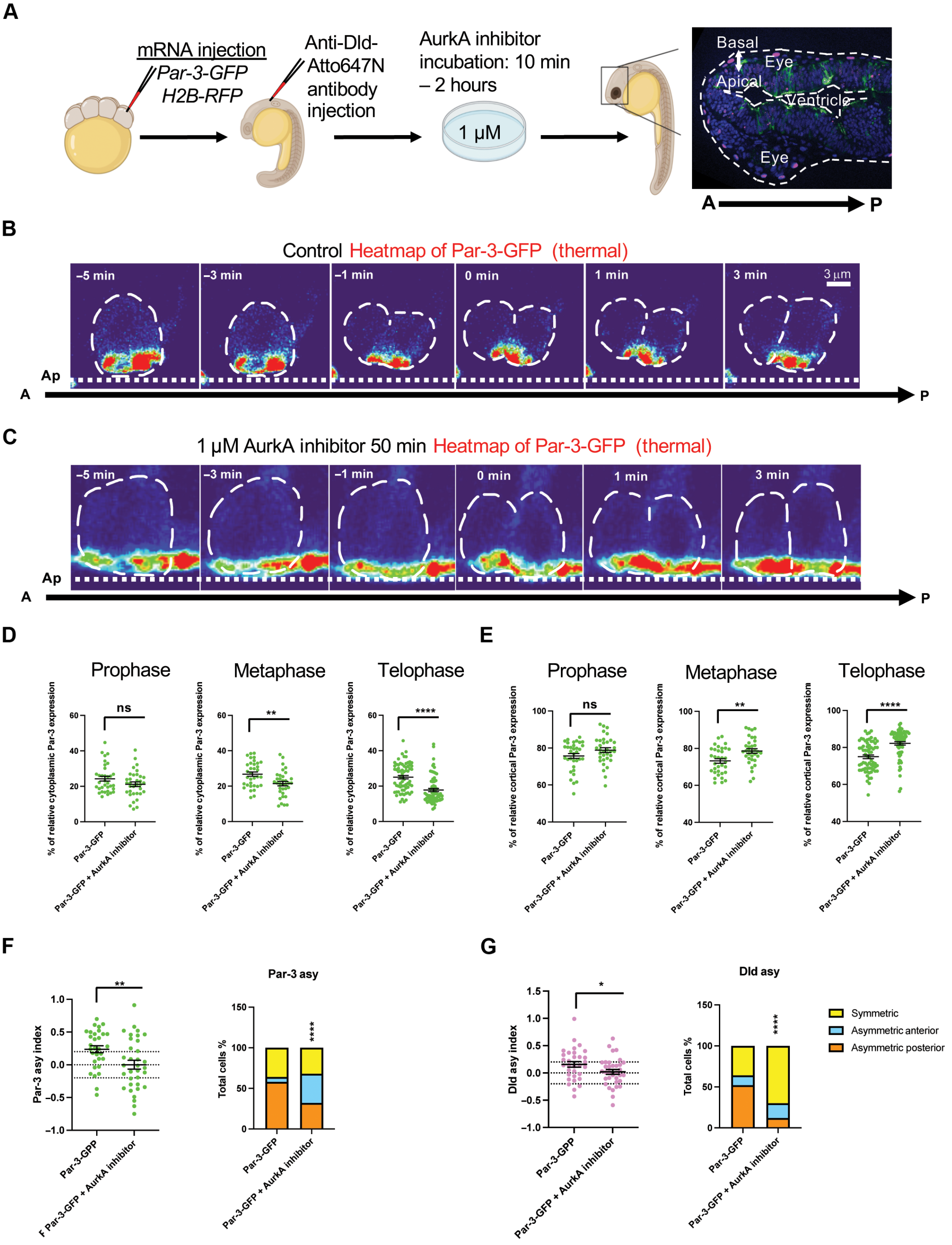

Fig. 7. Inhibition of AurkA reduces cytoplasmic Par-3 and disrupts cortical Par-3 and Dld asymmetry. (**A**) Experimental schematic. Embryos are injected with mRNA (~200 pg) at the 16/32-cell stage to achieve sparse labeling, followed by Dld antibody uptake at 20 hpf and treatment with 1 μM AurkA inhibitor (MK-5108) for 10 min to 2 hours, and the 24- to 30-hpf zebrafish forebrain region is imaged. A zoomed-in confocal image of a 28-hpf zebrafish forebrain (dorsal view) under a 40× objective. DNA is marked by H2B-RFP (pseudocolored in blue), Par-3-GFP (green), and internalized Dld (magenta). (**B** and **C**) Time-lapse sequence of images showing the dynamics of internalized Dld and Par-3-GFP in mitotic RGPs. The time of 3 min denotes the telophase when asymmetry indices are calculated. The time interval between each volume of *z*-stacks is 20 s, and the total acquisition time is 30 min. All images shown are MIP of three confocal *z*-stacks (1-μm *z*-step). (B) Control condition: Par-3-GFP time-lapse image showing the dynamics of internalized Dld and Par-3-GFP in mitotic RGPs. (C) Condition: time-lapse sequence of images of 1 μM AurkA Inhibitor for 50 min in mitotic RGPs. Par-3 and Dld asymmetry was disrupted. (**D** to **G**) Unpaired *t* test compared to control. (D) Quantification. Percent relative cytoplasmic Par-3 expression was measured at the prophase, metaphase, and telophase using Fiji. (E) Quantification. Percent relative cortical Par-3 expression was measured at the prophase, metaphase, and telophase using Fiji. (F) Asymmetry indices of Par-3-GFP. The dotted lines indicate the threshold of |0.2| for calling asymmetry. (G) Asymmetry indices of internalized Dld (right) in RGPs expressing different forms of Par-3. $*P < 0.05$, $**P < 0.01$, $***P < 0.001$, and $****P < 0.0001$; ns, not significant. For detailed statistics, see table S1. See table S2 for the representative image signal values compared to the median signal values.

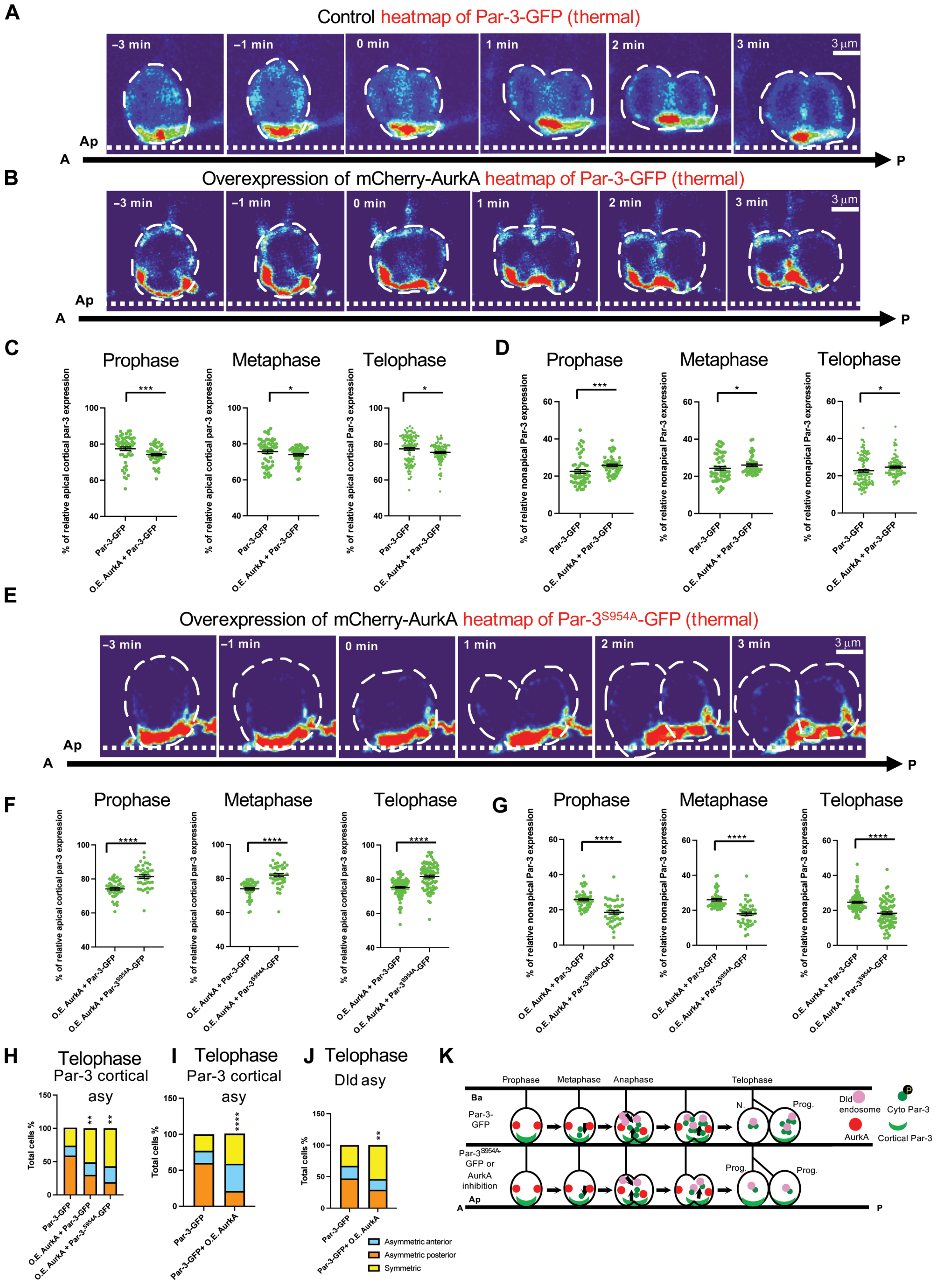

Fig. 8. Overexpression of AurkA results in an increase in cytoplasmic Par-3 and disrupts cortical Par-3 and Dld asymmetry. (**A**) Time-lapse sequence of images showing Par-3-GFP (200 pg) (GFP only in the heatmap) in mitotic RGPs. (**B**) Overexpression (O.E.) of AurkA + Par-3-GFP (400 and 200 pg, respectively) in mitotic RGPs. (**C**) Quantification. Apical cortical Par-3 expression was measured during the prophase, metaphase, and telophase in mitotic RGPs. (**D**) Nonapical Par-3 (cytoplasmic) expression was measured during the prophase, metaphase, and telophase in mitotic RGPs. (**E**) Time-lapse sequence of images showing overexpression of AurkA + Par-3^{S954A}-GFP (400 and 200 pg, respectively) (GFP only in the heatmap) in mitotic RGPs. (**F**) Quantification. Apical cortical Par-3 expression was measured during the prophase, metaphase, and telophase in mitotic RGPs. (**G**) Nonapical Par-3 (cytoplasmic) expression was measured during the prophase, metaphase, and telophase in mitotic RGPs. (**H** to **J**) Bar graphs represent Par-3 and Dld RGP divisions. (**K**) Model. N, neuron; Prog, progenitor; Ap, apical; Ba, basal; A, anterior; P, posterior. $*P < 0.05$, $**P < 0.01$, $***P < 0.001$, and $****P < 0.0001$; ns, not significant. For detailed statistics, see table S1. See table S2 for the representative image signal values compared to the median signal values.

embryonic and brain development upon ubiquitous expression of Par-3^{S954A}-GFP, the knockin mutant may have early developmental defects that preclude meaningful analysis and interpretation of RGP division. Future development of conditional knockin approaches will help address this and enable studies of RGP divisions at later stages.

Compared to the cortical Par-3-GFP signal, the cytoplasmic Par-3-GFP signal is low. Despite a low level, our previous study has shown that cytoplasmic Par-3 engages the dynein motor complex to colocalize on the Dld endosomes (*23*). Moreover, previous studies have uncovered considerable heterogeneity in gene expression and division modes across RGPs (*14*, *23*). As measurement of absolute cytoplasmic Par-3-GFP signals resulted in no clear patterns in relation to altered AurkA phosphorylation sites, we quantified relative rather than absolute Par-3-GFP signals, serving to normalize variations among RGPs, to the best extent that we can. Using this method, we detected significant reduction of cytoplasmic Par-3 when specific AurkA phosphorylation sites [S2A (Ser^2→Ala) and Ser^{954}] were disrupted. While the mean differences between experimental groups appear small, likely due to the biological heterogeneity of RGPs (e.g., only a subset of RGPs may be regulated by AurkA), we believe that the observed differences are not only statistically significant but also biologically meaningful, because the effects were observed in Par-3^{S2A}-GFP– and Par-3^{S954A}-GFP–expressing groups but not in Par-3^{S227A}-GFP–expressing groups. Moreover, these statistically significant effects were linked to their biological effects on brain development, Dld asymmetry, and daughter cell fate, as these biological effects were observed in Par-3^{S2A}-GFP– and Par-3^{S954A}-GFP–expressing groups but not in Par-3^{S227A}-GFP–expressing groups. Such "mild" but statistically significant findings are often observed in complex biological systems, e.g., in the study of behavioral phenotypes. Together, the low cytoplasmic Par-3-GFP signal and RGP heterogeneity make the intergroup differences of cytoplasmic and cortical Par-3-GFP signals appear small, but they are nevertheless biologically meaningful.

Using MO to knock down endogenous Par-3 while expressing Par-3-GFP, we were able to enhance the visualization of cytoplasmic Par-3-GFP and detect a large assembly, which contains Par-3-GFP colocalizing with many Dld endosomes and moves toward the posterior side. This observation suggests that rather than moving on an individual basis, Dld endosomes might be assembled into a larger structure that displays polarized dynamics. The nature of this large assembly and whether it is present in WT RGPs are unknown and require further investigations.

Our data showed that the S954A mutant had decreased cytoplasmic presence and dominant negatively interfered with embryonic development, RGP ACD, and progenitor fate. The nature of this dominant-negative effect remains mysterious. Our data are consistent with the idea that S954A interferes with the localization or the function of endogenous Par-3. For instance, it may trap endogenous Par-3 on the cell cortex through oligomeric complex formation mediated by the N-terminal domain of Par-3, or alternatively, it may trap other essential proteins on the cell cortex that render endogenous Par-3 nonfunctional. Future experiments are necessary to test this.

How might phosphorylation of Par-3 at Ser^{954} by AurkA increase the presence of Par-3 in the cytoplasm? We speculate that such phosphorylation may disrupt Par-3 interactions with other cortical proteins such as Par-6 or aPKC, thereby releasing it from the cortex. Once in the cytoplasm, Ser^{954}-phosphorylated Par-3 may interact with other proteins such as dynein motor and endosome-associated proteins.

Intriguingly, phosphorylation of Par-3 at Ser^{954} by AurkA appears not only to affect the cytoplasmic presence of Par-3 but also to affect the cortical asymmetry of Par-3. How this may be accomplished remains unclear. We postulate two possible mechanisms. One involves the initial deployment of phosphorylated Par-3 to the cytoplasm and subsequent return of dephosphorylated Par-3 back to the cortex preferentially on the posterior side of the cell. Alternatively, phosphorylated Par-3 may travel within the cortical domain in addition to being deployed into the cytoplasm, leading to posterior enrichment. Future experiments are required to test these hypotheses.

MATERIALS AND METHODS

Experimental design

Mitotic RGPs in the developing zebrafish forebrain during active neurogenesis were analyzed using a combination of in vivo time-lapse imaging, molecular genetics, pharmacology, and biochemistry, which has uncovered the role of Par-3 phosphorylation during ACD in RGPs.

Zebrafish strains and maintenance

WT embryos were obtained from natural spawning of AB adults, staged, and maintained according to established protocols (*47*). Embryos were raised at 28.5°C in 0.3× Danieau's embryo medium [30× Danieau's embryo medium contains 1740 mM NaCl, 21 mM KCl, 12 mM $MgSO_4 \cdot 7H_2O$, 18 mM $Ca(NO_3)_2$, and 150 mM Hepes buffer]. Embryonic ages were described as hpf. The following zebrafish mutants and transgenic lines were used: Tg[ef1a:Myr-Tdtomato] and Tg[b-actin2:H2B-HaloTag] (*48*), Halo Tag ligand, and Janelia Flour 646 (1:1000) for 2 hours before imaging. All animal experiments were approved by the Institutional Animal Care and Use Committee at the University of California, San Francisco, US (approval number: AN194551).

Morpholinos

Knockdown experiments were carried out using previously characterized translational blocking antisense MOs: pard3ab/par-3 MO (5′-TCA AAG GCT CCC GTG CTC TGG TGT C-3′) (*11*, *12*, *14*, *23*, *49*). All MOs were stored at 300 mM in distilled water. Standard control MO (5′-CCT CTT ACC TCA GTT ACA ATT TAT A-3′) was used as the injection control (Gene Tools). For microinjection, ~4 nl of the diluted MO at 100 mM in the injection mixture containing 0.05% phenyl red (corresponding to 4 ng of MOs) was injected into the yolk of one- to four-cell stage embryos.

DNA plasmids and complementary DNA preparation

Plasmid DNAs (pCS2-H2B-mRFP) were prepared as previously described (*14*, *50*). The pCS2-par-3-GFP plasmid was a gift from J. von Trotha (*10*). The pCS2-GFP-centrin plasmid was a gift from W. A. Harris (*51*). pCS2-mCherry-AurkA was a gift from H.-Y. Jeon (*33*). pCS2-Par-3-SA-GFP (Ser^{227} and Ser^{954} converted to Ala^{227} and Ala^{954}) and pCS2-Par-3-SD-GFP (Ser^{227} and Ser^{954} converted to Asp^{227} and Asp^{954}) were designed by S.G. and sent to VectorBuilder for plasmid construction. Single phosphor mutants pCS2-Par-3-S227A-GFP and pCS2-Par-3-S954A-GFP were cloned using Gibson Assembly (NEBuilder). For all par-3-GFP, GFP is at the 3′ end of

Par-3 protein. For GFP-centrin, GFP is at the 5′ end of centrin. For mCherry-AurkA, mCherry is at the 5′ end of AurkA.

mRNA synthesis and microinjection

Plasmids (pCS2-H2B-mRFP, pCS2-Par-3-GFP, pCS2-Par-3-SA-GFP, pCS2-Par-3-SD-GFP, pCS2-Par-3-S227A-GFP, pCS2-Par-3-S954A-GFP, pCS2-mCherry-AurkA, and pCS2-GFP-centrin) were linearized by restriction enzyme Not I digestion. Not I–linearized plasmids were purified (QIAquick Gel Extraction Kit), and the 5′-capped mRNAs were synthesized using the SP6 mMessenger mMachine Kit (Ambion). For GFP-centrin, H2B-mRFP, and all Par-3-GFP mRNA injections, 4 nl of mRNAs at 0.2 to 0.5 μg/μl was mixed with an equal volume of injection buffer containing 0.05% phenyl red and injected into the yolk of one- to four-cell stage embryos. For all Par3-GFP mRNA injections, the mRNAs were injected into single cells at the 32- to 64-cell stages to obtain mosaic expression. All injections were done with an injector (Narishige, Tokyo, Japan) and a micromanipulator (WPI PV830 Pneumatic Pico Pump).

Anti-Dld antibody uptake assay

Anti-mouse immunoglobulin G (IgG)–Atto647N (Sigma-Aldrich, 50185) was used for labeling the mouse monoclonal anti-Dld antibody (Abcam, ab73331). For antibody conjugation, 1 μl of anti-Dld antibody (0.5 mg/ml) was mixed with 2.5 μl of anti-mouse IgG-Atto647N antibody (1 mg/ml) and incubated at room temperature for 30 min or on ice for 2 to 3 hours. After incubation, 2.5 μl of blocking buffer [mouse IgG (10 mg/ml) with 5 mM azide] and 0.5 μl of 0.5% phenol red (Sigma-Aldrich, P0290) were added for blocking the unconjugated anti-mouse IgG-Atto647N and vortexed thoroughly. Mixtures without the anti-Dld antibody were used as control. Before microinjection, 24- to 26-hpf embryos were anesthetized in the Danieau medium supplemented with 0.003% tricaine followed by embedding in 1.2% low–melting point agarose. Ten nanoliters of labeled Dld antibody was injected into the hindbrain ventricle. The phenol red indicator shows the diffusion of the antibody mixture into the forebrain ventricle. The injected embryos were then released from agarose and cultured in the Danieau medium for 2 hours before imaging.

Pharmacology

Zebrafish embryos were treated with an AurkA inhibitor (MedChemExpress, MK-5108, HY-13252, CAS no. 1010085-13-8) from 22 to 24 hpf for various durations before imaging (10, 20, 30, 40, 50, 60, and 120 min). Dld antibody uptake assay was performed before vehicle (dimethyl sulfoxide)–treated control and 1 μM AurkA inhibitor–treated embryos were then embedded in 1.5% low–melting point agarose in the Danieau medium supplemented with 1 μM AurkA inhibitor and 0.003% tricaine for in vivo time-lapse imaging.

Antibodies, Western blotting, and immunocytochemistry

Primary antibodies used in this study were as follows: mouse anti-Dld [Abcam, ab73331; Research Resource Identifier (RRID): AB_1268496; chicken anti-GFP (Abcam, ab13970; RRID: AB_300798; lot GR3190550-20; 1:500 dilution for immunostaining), rabbit anti–Par-3 (Millipore 07-330; RRID: AB_2101325; lot 3322358; 1:500 for immunostaining), and anti-HuC (Invitrogen A-21271; RRID: AB_221448; 1:1000 for immunostaining). For EDU labeling, the Click-iT EdU Alexa Flour 555 kit (C10338; lot 2491411) contains all components needed to label DNA-synthesizing cells and to detect EDU incorporated into DNA stained according to the manufacturer's protocol (Invitrogen). For EDU labeling, embryos are embedded in 1.2% low-melt agarose, and EDU and 0.5 μl of 0.5% phenol red (Sigma-Aldrich, P0290) were added to the injection mixture and administered into the yolk sac with 4.2 nl of 50 μM EDU at 18 hpf into the yolk sac.

For the preparation of cryosections, 28- and 36-hpf embryos were fixed overnight at 4°C in phosphate-buffered saline buffer with 4% paraformaldehyde. Fixed embryos were washed abundantly with phosphate-buffered saline and then cryoprotected in 30% sucrose overnight at 4°C. Embryos were then embedded with optimum cutting temperature compound (Tissue-Tek) and transferred to plastic molds. After orienting the embryos to proper positions in the mold, the block was frozen on dry ice and then stored at −80°C up to several months. Frozen blocks were then cut into 18-μm sections on a cryostat (Leica) and mounted on Superfrost Plus slides (Thermo Fisher Scientific). The slides were dried at room temperature for 2 to 3 hours and then stored at −80°C until use.

In vitro–translated proteins and in vitro immunoprecipitation

The pCS2+-Par-3-GFP plasmid and phosphor mutants (pCS2+-Par-3-S227A-GFP, pCS2+-Par-3-S954A-GFP, and pCS2+-Par-3-SA-GFP) plasmids were generated in TNT SP6 High-Yield Protein Expression System (Promega) according to the manufacturer's instructions. Briefly, 1 μg of DNA was mixed with a master mix of TNT Sp6 and methionine or ^{35}S-labeled methionine, incubated at 25°C for 2 hours, and then mixed with the ChromoTek GFP-Trap_ Agarose beads (Proteintech). The beads were then washed twice with ice cold wash buffer, in vitro kinase assay was performed, and then samples were resuspended in 4× Laemmli sample buffer and boiled for 10 min at 95°C before loading onto the SDS–polyacrylamide gel electrophoresis (SDS-PAGE) gels.

In vitro kinase assay

For multisite phosphorylation analysis of WT and mutant Par-3, phosphorylation reactions were supplemented with [γ-^{32}P]-adenosine 5′-triphosphate {γ-^{32}P]-ATP} (Hartmann Analytic). Reactions were stopped at 5, 15, and 60 min by pipetting an aliquot of SDS-PAGE into sample buffer (1 mol of Hepes, pH 7.5, 2 mol of NaCl, 1 mol of $MgCl_2$, 100 μM dithiothreitol, and H_2O). Reactions were separated on 7.5% SDS (Bio-Rad). ^{32}P phosphorylation signals were detected using an Amersham Typhoon 5 Biomolecular Imager (GE Healthcare Life Sciences) and quantified using ImageQuant TL (Amersham Biosciences). Human Aurora Kinase A-His Tag Recombinant Protein (250 nmol; Invitrogen, PR5935A) was used.

In vivo time-lapse imaging

In vivo time-lapse imaging was done using a confocal microscope (Nikon CSU-W1 Spinning Disk/High Speed Widefield confocal microscopy and Weill CSU-W1 SoRA Spinning Disk Confocal) with a 40× water immersion objective. Embryos were mounted with 1.5% low–melting point agarose (0.3× Danieau medium and 0.003% tricaine) in glass-bottom culture dishes (MatTek; 35 mm) with the dorsal forebrain facing the coverslip. For in vivo time-lapse imaging of internalized Dld or Par3-GFP in dividing RGPs of Tg[ef1a:Myr-Tdtomato], *z*-stacks with 20 to 30 *z*-planes were acquired consecutively at a 1-μm *z*-step for each embryonic forebrain region. The exposure time for each fluorescent channel was set at 200 ms by choosing the sequential channel scanning mode for each z-plane. The interval between each z-stack was 20 s. Usually, 90 volumes of z-stacks were captured for each time-lapse imaging, and the duration spanned about 35 min. Imaging data were collected using identical microscope settings across different embryos/conditions.

Image analyses

All the confocal imaging stacks were captured and processed using Micro-Manager 2.0 gamma (uManager, University of California) and ImageJ. All mitotic RGPs (based on the H2B-RFP signal) in the image stacks were analyzed if they expressed Par-3 reporters (or other markers of interest) and had most of their mitotic cell cycles captured during the imaging session. Maximum intensity projection of three z-planes (1-μm z-step) was applied to the three-dimensional image stacks to cover the entire RGP. Each RGP at every time frame was manually segmented according to cell membrane labeling, as previously described by Zhao *et al.* (*23*). Each image was processed in an identical manner to optimize brightness and contrast using the autocorrect function in ImageJ, followed by image sharpening. Background noise was minimized by adjusting the brightness and contrast settings in ImageJ. Signals for cytoplasmic Par-3, cortical Par-3, internalized Dld, and the AurkA reporter were subsequently analyzed at various cell cycle stages, including prophase, metaphase, and telophase, as depicted in the figures. CellProfiler was used for analyzing the immunocytochemistry of the EDU pulse-chase cryosections, 21 μm was taken, and the brightest (1-μm z-step) was taken, processed, and analyzed through CellProfiler.

Quantification and statistical analysis

The number of times each experiment was repeated was provided in the figures or figure legends. For live imaging, one or multiple RGPs were analyzed from each embryo, depending on the number of mitotic RGPs that were present in each image stack. No statistical methods were used to predetermine sample size. Sample size was determined to be adequate based on the magnitude and consistency of measurable differences between groups. No randomization of samples was performed. Embryos used in the analyses were age matched between control and experimental conditions, and sex cannot be discerned at these embryonic stages. Investigators were not blinded to chemically or genetically perturbed conditions during experiments. Data are quantitatively analyzed. Statistical analyses were carried out using Prism 10 version 10.1.1: The mean value with SEM was labeled in the graphs. The two-tailed unpaired t test and two-tailed Mann-Whitney test were used to assess significance. The one-way analysis of variance (ANOVA) with a post hoc comparison was used to assess significance as well. Chi-square analyses were also applied, as previously described by Zhao *et al.* (*23*).

Measurement of asymmetry index

The total fluorescence intensity of internalized Dld (or Par-3-GFP) in paired daughter cells immediately after abscission (i.e., at the telophase of mother RGP division) was measured by ImageJ. To quantitatively describe the distribution, the normalized ratio of fluorescence between the two newly formed daughter cells was calculated as follows

$$X = \frac{\sum_{i=1}^{n} (\text{Dld})\text{P} - \sum_{i=1}^{n} (\text{Dld})\text{A}}{\sum_{i=1}^{n} (\text{Dld})\text{P} + \sum_{i=1}^{n} (\text{Dld})\text{A}}$$

$\Sigma(\text{Dld})\text{P}$ means the total intensity in the posterior daughter cell, and $\Sigma(\text{Dld})\text{A}$ means the total intensity in the anterior daughter cell. "0" indicates perfect symmetry, and "1" or "−1" indicates absolute asymmetry (posterior or anterior, respectively). For filtering out potential noise, we defined asymmetry when $\Sigma(\text{Dld})\text{P}$ is 50% more or less than $\Sigma(\text{Dld})\text{A}$, as has been previously used for quantifying Par-3 asymmetry (*13*) and internalized Dld–containing Sara endosome asymmetry (*15*). It means that when $X \geq 0.2$, Dld endosomes (and Par-3-GFP) are considered asymmetric with more in the posterior daughter, and when $X \leq -0.2$, they are considered asymmetric with more in the anterior. The asymmetry index for Par3-GFP included both membrane and cytoplasmic fluorescence.

Supplementary Materials

The PDF file includes:
Figs. S1 to S10
Table S1
Legend for table S2
Legends for movies S1 to S14

Other Supplementary Material for this manuscript includes the following:
Table S2
Movies S1 to S14

REFERENCES AND NOTES

1. J. A. Knoblich, Asymmetric cell division: Recent developments and their implications for tumour biology. *Nat. Rev. Mol. Cell Biol.* **11**, 849–860 (2010).
2. K. J. Yong, B. Yan, The relevance of symmetric and asymmetric cell divisions to human central nervous system diseases. *J. Clin. Neurosci.* **18**, 458–463 (2011).
3. Z. Li, Y. Y. Zhang, H. Zhang, J. Yang, Y. Chen, H. Lu, Asymmetric cell division and tumor heterogeneity. *Front. Cell Dev. Biol.* **10**, 938685 (2022).
4. M. C. Florian, H. Geiger, Concise review: Polarity in stem cells, disease, and aging. *Stem Cells* **28**, 1623–1629 (2010).
5. V. Aranda, M. E. Nolan, S. K. Muthuswamy, Par complex in cancer: A regulator of normal cell polarity joins the dark side. *Oncogene* **27**, 6878–6887 (2008).
6. B. Etemad-Moghadam, S. Guo, K. J. Kemphues, Asymmetrically distributed PAR-3 protein contributes to cell polarity and spindle alignment in early C. elegans embryos. *Cell* **83**, 743–752 (1995).
7. S. Guo, K. J. Kemphues, Molecular genetics of asymmetric cleavage in the early *Caenorhabditis elegans* embryo. *Curr. Opin. Genet. Dev.* **6**, 408–415 (1996).
8. S. Guo, K. J. Kemphues, *par-1*, a gene required for establishing polarity in C. elegans embryos, encodes a putative Ser/Thr kinase that is asymmetrically distributed. *Cell* **81**, 611–620 (1995).
9. L. S. Rose, K. J. Kemphues, Early patterning of the *C. elegans* embryo. *Annu. Rev. Genet.* **32**, 521–545 (1998).
10. J. W. von Trotha, J. A. Campos-Ortega, A. M. Reugels, Apical localization of ASIP/PAR-3:EGFP in zebrafish neuroepithelial cells involves the oligomerization domain CR1, the PDZ domains, and the C-terminal portion of the protein. *Dev. Dyn.* **235**, 967–977 (2008).
11. M. Tawk, C. Araya, D. A. Lyons, A. M. Reugels, G. C. Girdler, P. R. Bayley, D. R. Hyde, M. Tada, J. D. W. Clarke, A mirror-symmetric cell division that orchestrates neuroepithelial morphogenesis. *Nature* **446**, 797–800 (2007).
12. P. Alexandre, A. M. Reugels, D. Barker, E. Blanc, J. D. W. Clarke, Neurons derive from the more apical daughter in asymmetric divisions in the zebrafish neural tube. *Nat. Neurosci.* **13**, 673–679 (2010).
13. R. S. Bultje, D. R. Castaneda-Castellanos, L. Y. Jan, Y.-N. Jan, A. R. Kriegstein, S.-H. Shi, Mammalian Par3 regulates progenitor cell asymmetric division via notch signaling in the developing neocortex. *Neuron* **63**, 189–202 (2009).
14. Z. Dong, N. Yang, S.-Y. Yeo, A. Chitnis, S. Guo, Intralineage directional notch signaling regulates self-renewal and differentiation of asymmetrically dividing radial glia. *Neuron* **74**, 65–78 (2012).
15. S. Kressmann, C. Campos, I. Castanon, M. Fürthauer, M. González-Gaitán, Directional Notch trafficking in Sara endosomes during asymmetric cell division in the spinal cord. *Nat. Cell Biol.* **17**, 333–339 (2015).
16. K. I. Mizutani, K. Yoon, L. Dang, A. Tokunaga, N. Gaiano, Differential Notch signalling distinguishes neural stem cells from intermediate progenitors. *Nature* **449**, 351–355 (2007).

17. S. E. Williams, S. Beronja, H. A. Pasolli, E. Fuchs, Asymmetric cell divisions promote Notch-dependent epidermal differentiation. *Nature* **470**, 353–358 (2011).
18. S. Artavanis-Tsakonas, M. D. Rand, R. J. Lake, Notch signaling: Cell fate control and signal integration in development. *Science* **284**, 770–776 (1999).
19. N. Gaiano, G. Fishell, The role of Notch in promoting glial and neural stem cell fates. *Annu. Rev. Neurosci.* **25**, 471–490 (2002).
20. R. Halaoui, L. McCaffrey, Rewiring cell polarity signaling in cancer. *Oncogene* **34**, 939–950 (2015).
21. M. D. Taylor, H. Poppleton, C. Fuller, X. Su, Y. Liu, P. Jensen, S. Magdaleno, J. Dalton, C. Calabrese, J. Board, T. Macdonald, J. Rutka, A. Guha, A. Gajjar, T. Curran, R. J. Gilbertson, Radial glia cells are candidate stem cells of ependymoma. *Cancer Cell* **8**, 323–335 (2005).
22. W. A. Liu, S. Chen, Z. Li, C. H. Lee, G. Mirzaa, W. B. Dobyns, M. E. Ross, J. Zhang, S.-H. Shi, PARD3 dysfunction in conjunction with dynamic HIPPO signaling drives cortical enlargement with massive heterotopia. *Genes Dev.* **32**, 763–780 (2018).
23. X. Zhao, J. Q. Garcia, K. Tong, X. Chen, B. Yang, Q. Li, Z. Dai, X. Shi, I. B. Seiple, B. Huang, S. Guo, Polarized endosome dynamics engage cytosolic Par-3 and dynein during asymmetric division. *Sci. Adv.* **7**, eabg1244 (2021).
24. F. Coumailleau, M. Fürthauer, J. A. Knoblich, M. González-Gaitán, Directional Delta and Notch trafficking in Sara endosomes during asymmetric cell division. *Nature* **458**, 1051–1055 (2009).
25. E. Derivery, C. Seum, A. Daeden, S. Loubéry, L. Holtzer, F. Jülicher, M. Gonzalez-Gaitan, Polarized endosome dynamics by spindle asymmetry during asymmetric cell division. *Nature* **528**, 280–285 (2015).
26. B. Li, H. Kim, M. Beers, K. Kemphues, Different domains of *C. elegans* PAR-3 are required at different times in development. *Dev. Biol.* **344**, 745–757 (2010).
27. R. W. Holly, K. E. Prehoda, Phosphorylation of Par-3 by atypical protein kinase C and competition between its substrates. *Dev. Cell* **49**, 678–679 (2019).
28. R. W. Holly, K. Jones, K. E. Prehoda, A conserved PDZ-binding motif in aPKC interacts with Par-3 and mediates cortical polarity. *Curr. Biol.* **30**, 893–898.e5 (2020).
29. D. Lin, A. S. Edwards, J. P. Fawcett, G. Mbamalu, J. D. Scott, T. Pawson, A mammalian PAR-3-PAR-6 complex implicated in Cdc42/Rac1 and aPKC signalling and cell polarity. *Nat. Cell Biol.* **2**, 540–547 (2000).
30. E. Morais-de-Sá, V. Mirouse, D. St Johnston, aPKC phosphorylation of bazooka defines the apical/lateral border in *Drosophila* epithelial cells. *Cell* **141**, 509–523 (2010).
31. F. Motegi, S. Zonies, Y. Hao, A. A. Cuenca, E. Griffin, G. Seydoux, Microtubules induce self-organization of polarized PAR domains in *Caenorhabditis elegans* zygotes. *Nat. Cell Biol.* **13**, 1361–1367 (2011).
32. D. J. Dickinson, F. Schwager, L. Pintard, M. Gotta, B. Goldstein, A single-cell biochemistry approach reveals PAR complex dynamics during cell polarization. *Dev. Cell* **42**, 416–434.e11 (2017).
33. H.-Y. Jeon, H. Lee, Depletion of Aurora-A in zebrafish causes growth retardation due to mitotic delay and p53-dependent cell death. *FEBS J.* **280**, 1518–1530 (2013).
34. J. D. Reich, L. Hubatsch, R. Illukkumbura, F. Peglion, T. Bland, N. Hirani, N. W. Goehring, Regulated activation of the PAR polarity network ensures a timely and specific response to spatial cues. *Curr. Biol.* **29**, 1911–1923.e5 (2019).
35. F. Wirtz-Peitz, T. Nishimura, J. A. Knoblich, Linking cell cycle to asymmetric division: Aurora-A phosphorylates the Par complex to regulate numb localization. *Cell* **135**, 161–173 (2008).
36. M. R. Khazaei, A. W. Püschel, Phosphorylation of the Par polarity complex protein Par3 at Serine 962 is mediated by Aurora A and regulates its function in neuronal polarity. *J. Biol. Chem.* **284**, 33571–33579 (2009).
37. X. Zhao, J. Garcia, L. A. Royer, S. Guo, Colocalization analysis for cryosectioned and immunostained tissue samples with or without label retention expansion microscopy (LR-ExM) by JACoP. *Bio Protoc.* **12**, e4336 (2022).
38. K. Tong, M. Wagle, S. Guo, Antibody uptake assay in the embryonic zebrafish forebrain to study notch signaling dynamics in neural progenitor cells in vivo. *Methods Mol. Biol.* **1576**, 273–281 (2019).
39. X. Zhao, S. Guo, Antibody uptake assay for tracking Notch/Delta endocytosis during the asymmetric division of zebrafish radial glia progenitors. *J. Vis. Exp.*, 10.3791/65030, (2023).
40. I. M. Cheeseman, S. Anderson, M. Jwa, E. M. Green, J.-S. Kang, J. R. Yates Iii, C. S. M. Chan, D. G. Drubin, G. Barnes, Phospho-regulation of kinetochore-microtubule attachments by the Aurora kinase Ipl1p. *Cell* **111**, 163–172 (2002).
41. S. Ferrari, O. Marin, M. A. Pagano, F. Meggio, D. Hess, M. El-Shemerly, A. Krystyniak, L. A. Pinna, Aurora-A site specificity: A study with synthetic peptide substrates. *Biochem. J.* **390**, 293–302 (2005).
42. K. Petri, W. Zhang, J. Ma, A. Schmidts, H. Lee, J. E. Horng, D. Y. Kim, I. C. Kurt, K. Clement, J. Y. Hsu, L. Pinello, M. V. Maus, J. K. Joung, J.-R. J. Yeh, CRISPR prime editing with ribonucleoprotein complexes in zebrafish and primary human cells. *Nat. Biotechnol.* **40**, 189–193 (2022).
43. N. Yang, Z. Dong, S. Guo, Fezf2 regulates multilineage neuronal differentiation through activating basic helix-loop-helix and homeodomain genes in the zebrafish ventral forebrain. *J. Neurosci.* **32**, 10940–10948 (2012).
44. A. A. Leontovich, J. L. Salisbury, M. Veroux, T. Tallarita, D. Billadeau, J. McCubrey, J. Ingle, E. Galanis, A. B. D'Assoro, Inhibition of Cdk2 activity decreases Aurora-A kinase centrosomal localization and prevents centrosome amplification in breast cancer cells. *Oncol. Rep.* **29**, 1785–1788 (2013).
45. T. Shimomura, S. Hasako, Y. Nakatsuru, T. Mita, K. Ichikawa, T. Kodera, T. Sakai, T. Nambu, M. Miyamoto, I. Takahashi, S. Miki, N. Kawanishi, M. Ohkubo, H. Kotani, Y. Iwasawa, MK-5108, a highly selective Aurora-A kinase inhibitor, shows antitumor activity alone and in combination with docetaxel. *Mol. Cancer Ther.* **9**, 157–166 (2010).
46. J. Dagher, F. Dugay, N. Rioux-Leclercq, G. Verhoest, E. Oger, K. Bensalah, F. Cabillic, F. Jouan, S. F. Kammerer-Jacquet, P. Fergelot, C. Vigneau, Y. Arlot-Bonnemains, M. A. Belaud-Rotureau, Cytoplasmic PAR-3 protein expression is associated with adverse prognostic factors in clear cell renal cell carcinoma and independently impacts survival. *Hum. Pathol.* **45**, 1639–1646 (2014).
47. C. B. Kimmel, W. W. Ballard, S. R. Kimmel, B. Ullmann, T. F. Schilling, Stages of embryonic development of the zebrafish. *Dev. Dyn.* **203**, 253–310 (1995).
48. Y. Wan, Z. Wei, L. L. Looger, M. Koyama, S. Druckmann, P. J. Keller, Single-cell reconstruction of emerging population activity in an entire developing circuit. *Cell* **179**, 355–372.e23 (2019).
49. X. Wei, Y. Cheng, Y. Luo, X. Shi, S. Nelson, D. R. Hyde, The zebrafish Pard3 ortholog is required for separation of the eye fields and retinal lamination. *Dev. Biol.* **269**, 286–301 (2004).
50. Z. Dong, M. Wagle, S. Guo, Time-lapse live imaging of clonally related neural progenitor cells in the developing zebrafish forebrain. *J. Vis. Exp.*, 2594 (2011).
51. F. R. Zolessi, L. Poggi, C. J. Wilkinson, C. B. Chien, W. A. Harris, Polarization and orientation of retinal ganglion cells in vivo. *Neural Dev.* **1**, 2 (2006).

Acknowledgments: We thank M. Munchua and E. Lee for excellent animal care; Guo laboratory members for helpful discussions; and D. Larsen, K. Harrington, S. Kim, UCSF Nikon Imaging Center, and Weill Innovation Core for assistance with imaging and data analysis. **Funding:** This project was supported by NIH R01NS120218 and R21NS122053 (to S.G.), The Luis Zeh Fellowship and NIH R01NS120218 Diversity Supplement (to J.Q.G), and NIH R35-GM118053 (to D.O.M.). **Author contributions:** J.Q.G.: writing—original draft, conceptualization, investigation, writing—review and editing, methodology, resources, funding acquisition, data curation, validation, supervision, formal analysis, software, project administration, and visualization. S.G.: writing—original draft, conceptualization, writing—review and editing, methodology, resources, funding acquisition, validation, supervision, and project administration. X.Z.: writing—original draft, conceptualization, investigation, writing—review and editing, methodology, resources, data curation, validation, supervision, formal analysis, software, project administration, and visualization. D.O.M.: investigation, writing—review and editing, methodology, resources, funding acquisition, and supervision. H.N.: investigation, writing—review and editing, methodology, and resources. V.M.: investigation, writing—review and editing, methodology, resources, data curation, validation, formal analysis, software, project administration, and visualization. **Competing interests:** The authors declare that they have no competing interests. **Data and materials availability:** All data needed to evaluate the conclusions in the paper are present in the paper and/or the Supplementary Materials.

Submitted 10 May 2024
Accepted 25 February 2025
Published 14 May 2025
10.1126/sciadv.adq3858